

Model-Specific Task Similarity for Vision–Language Model Selection via Layer Conductance

Wei Yang^{1*} Hong Xie^{2*} Tao Tan³ Xin Li³ Defu Lian³ Enhong Chen³

Abstract

While open-sourced Vision-Language Models (VLMs) have proliferated, selecting the optimal pre-trained model for a specific downstream task remains challenging. Exhaustive evaluation is often infeasible due to computational constraints and data limitations in few-shot scenarios. Existing selection methods fail to fully address this: they either rely on data-intensive proxies or use symmetric textual descriptors that neglect the inherently directional and model-specific nature of transferability. To address this problem, we propose a framework that grounds model selection in the internal functional dynamics of the visual encoder. Our approach represents each task via layer-wise conductance and derives a target-conditioned block-importance distribution through entropy-regularized alignment. Building on this, we introduce Directional Conductance Divergence (DCD), an asymmetric metric that quantifies how effectively a source task covers the target’s salient functional blocks. This allows for predicting target model rankings by aggregating source-task ranks without direct inference. Experimental results on 48 VLMs across 21 datasets demonstrate that our method outperforms state-of-the-art baselines, achieving a 14.7% improvement in NDCG@5 over SWAB.

1. Introduction

VLMs pretrained on large-scale image–text pairs have become core engines for tasks such as visual understanding and embodied intelligence, particularly in zero-shot transfer scenarios (Radford et al., 2021; Ma et al., 2024; Zhang et al.,

¹School of AI and Data Science, University of Science and Technology of China, Hefei, China ²School of Computer Science and Technology, University of Science and Technology of China, Hefei, China ³School of Computer Science and Technology, University of Science and Technology of China, Hefei, China. Correspondence to: Hong Xie <hongx87@ustc.edu.cn>.

Preprint. February 3, 2026.

2024). With the rapid emergence of open-source VLMs spanning diverse architectures and pretraining strategies, selecting the most suitable pretrained model for a target task has become increasingly critical. Exhaustive evaluation is often infeasible, since target domains usually provide only a few or even no test data samples at all. Therefore, transferability estimation becomes the mainstream approach to crack this problem (Ding et al., 2024; Xue et al., 2024).

Transferability estimation is a central and long-standing problem in the transfer learning area (Ding et al., 2024; Xue et al., 2024). Though many methods were proposed, they fall short in the VLMs selection problem. More specifically, data-driven proxy metrics are unstable in few-shot regimes (You et al., 2021; Nguyen et al., 2020). Alternatively, prior task-centric formulations like LOVM (Zohar et al., 2023) and SWAB (Yi et al., 2024) estimate transferability by the embeddings of textual task descriptions. Target domain data free is one major merit of these methods, but it also leads to the performance bottleneck. This is because task similarity is inherently model-specific (Achille et al., 2019; Mehra et al., 2024). This results in the *data vs. performance* dilemma.

This paper develops an alternative to addressing the aforementioned dilemma. Our idea is inspired by practical scenarios that a few unlabeled target images are usually available in the target task. Though these unlabeled target images offers relatively weak visual signals, it turns out that they can elicit strong signals for estimating model-specific task similarity if done properly. To leverage them, we ground task relatedness in model-specific internal dynamics. Concretely, we represent each task by the layer-wise contribution profile of the model’s visual encoder, computed via layer conductance over coarse-grained blocks (Dhamdhere et al., 2019). This yields a lightweight, label-free, and inherently model-specific task representation, directly reflecting which functional blocks the target domain relies on.

Building on the above view, we derive a target-conditioned block-importance distribution via entropy-regularized alignment (Cuturi, 2013) and propose Directional Conductance Divergence (DCD), an asymmetric metric that captures whether source-task mechanisms cover target-critical blocks. Note the asymmetric property is desirable, since transfer is

inherently directional and model-specific: tasks that appear similar under one model’s representations may diverge under another (Achille et al., 2019). We then predict target-task rankings by aggregating source-task model rankings with DCD-induced similarity weights, avoiding direct target-task evaluation and enabling efficient few-shot selection. Under limited sampling, our approach achieves roughly a 15% improvement in NDCG@5 and $\tau@5$ over SWAB. The main contributions are:

- A model-specific task representation based on layer conductance of the visual encoder, requiring only a few unlabeled images from target tasks.
- DCD, a target-conditioned asymmetric transferability metric that captures directional coverage.
- A similarity-weighted rank aggregation scheme for target-task ranking without direct evaluation, validated across diverse VLMs and datasets.

2. Related Work

Vision–Language Models. Vision–Language Models (VLMs), trained via contrastive learning on large-scale image–text pairs, have become foundational to cross-modal representation learning (Radford et al., 2021). Prominent examples include CLIP (Radford et al., 2021), ALIGN (Jia et al., 2021), FLAVA (Singh et al., 2022), Florence (Yuan et al., 2021), and CoCa (Yu et al., 2022). Despite these advances, the performance of VLMs varies considerably across tasks and domains and often degrades under distribution shift (Zohar et al., 2023). Meanwhile, the rapid proliferation of open-source models, where each trained on distinct architectures and corpora, has given rise to a heterogeneous “VLMs Zoo” (Schuhmann et al., 2022; Ilharco et al., 2021; Wolf et al., 2020). In this landscape, strong benchmark results do not guarantee downstream effectiveness, shifting the central challenge from training a single universal model to selecting the most suitable VLM for a given target task. This work investigates efficient and reliable VLM selection from the zoo without exhaustive per-task evaluation.

Model Selection. A key challenge in deploying pre-trained models lies in estimating their transferability. Existing methods address it via proxy metrics such as H-Score (Bao et al., 2019), LogME (You et al., 2021) and LEEP (Nguyen et al., 2020), or through representation similarity such as Task2Vec (Achille et al., 2019) and Model Spider (Zhang et al., 2023). Unsupervised approaches further attempt to predict performance using only unlabeled data signals (Sun et al., 2021). However, these methods uniformly demand sufficient target-task data. This demand ill-suits VLMs, which are often deployed in zero-shot or few-shot scenarios (Zohar et al., 2023; Yi et al., 2024). Moreover, most prior work is de-

veloped for unimodal architectures and rarely accounts for VLMs’ multimodal nature.

Recent paradigms decouple VLM evaluation from labeled image. LOVM (Zohar et al., 2023) ranks VLMs using only textual task descriptions, while SWAB (Yi et al., 2024) advances this via an optimal transport framework that bridges modality and capability gaps across tasks. Parallel efforts like Model Label Learning (MLL) (Tan et al., 2025) further propose pre-assigning capability labels to VLMs to enable efficient selection and ensemble-based reuse for downstream adaptation. These methods pushed the frontier of state of the art, but they also have limitations that worth further investigation: they ignore the practical prevalence of few-shot settings where a small set of target images is available. In this regime, data-heavy methods yield unstable estimates, whereas text-only approaches waste informative visual cues already present in the available samples.

VLMs performance hinges on both visual representation quality and vision–language alignment (Radford et al., 2021; Yang et al., 2024). When limited target-domain images are available, leveraging these samples to reveal performance differences among candidate models becomes essential for reliable selection—a setting that remains largely unexplored. Furthermore, prior task-centric formulations (LOVM (Zohar et al., 2023) and SWAB (Yi et al., 2024)) embed tasks into text space to estimate transferability. This formulation overlooks the fact that task similarity is inherently model-specific (Achille et al., 2019; Mehra et al., 2024): tasks that appear similar under one model’s representations may diverge substantially under another, due to differences in architectural biases, pre-training objectives, and learned features. Recent empirical analysis (Sachdeva et al., 2025) reinforces this by mapping the complex, non-uniform patterns of positive and negative transfer across different VLM architectures. Ignoring this model-specific nature of task relatedness therefore leads to inaccurate transferability estimation, particularly across heterogeneous VLM collections. Motivated by these observations, we propose a VLMs selection framework tailored to few-shot and weakly supervised settings, which leverages limited visual evidence while explicitly modeling task relatedness in a model-specific manner.

Layer Conductance. Layer conductance is an attribution method that quantifies the contribution of intermediate-layer activations to model outputs (Dhamdhere et al., 2019; Sundararajan et al., 2017). It extends Integrated Gradients from input features to hidden representations, enabling principled attribution while satisfying axiomatic properties such as completeness. We show that layer conductance VLMs is effective in eliciting strong signals for estimating model-specific task similarity from unlabeled images.

3. Unlabeled Images Elicit Similarity Signals

This section motivates and validates the core premise of our approach that a small set of unlabeled target images can reveal reliable, model-specific signals of task relatedness, which align more closely with transferability than text-only semantic proxies.

Task Representations via Layer Conductance. We consider the setting that a few unlabeled images are available. A classical view in computer vision treats deep neural networks as cascaded filter banks that learn hierarchical representations through successive transformations (Zeiler & Fergus, 2014; Bau et al., 2017). Under this perspective, different layers capture distinct aspects of task-relevant information. If a task consistently relies on specific blocks (e.g., early texture-oriented stages versus later semantic stages), the distribution of layer contributions provides a compact summary of the task as perceived by the model. This intuition resonates with the task embedding paradigm of Task2Vec (Achille et al., 2019), which represents tasks through statistics of internal learning signals. We extend this to a model-specific formulation: rather than constructing a universal task graph, we characterize each task by its layer-wise dependency structure within a given VLM. Specifically, we use layer conductance (Dhamdhare et al., 2019; Sundararajan et al., 2017) to extract a block-wise contribution vector from the visual encoder. We assume that this distribution encodes intrinsic task semantics from the perspective of internal representations, providing a robust, model-specific basis for quantifying task similarity.

Task	Performance(Acc.) gap matrix G			Proxy gap matrix G'			Task
	A	B	C	A	B	C	
A	0	2	5	0	1.2	2.5	A
B	2	0	3	1.2	0	3.3	B
C	5	3	0	2.5	3.3	0	C

↓ *flatten upper triangle* ↓
 $\text{Vec}(G) = [2, 5, 3]$ $\text{Vec}(G') = [1.2, 2.5, 3.3]$
 $\rho = \text{Spearman}(\text{Vec}(G), \text{Vec}(G'))$
 larger $\rho \rightarrow$ more informative

Perf.: $G_{ij} = |\text{Acc}_i - \text{Acc}_j|$
 Semantic: $G'_{ij} = 1 - \cos(\text{emb}_i, \text{emb}_j)$
 Conductance: $G'_{ij} = \frac{1}{2}(D_m(i \rightarrow j) + D_m(j \rightarrow i))$

Figure 1. How we measure proxy reliability. We construct a performance gap matrix G with entries $G_{ij} = |\text{Acc}_i - \text{Acc}_j|$, and a proxy gap matrix G' from either semantic distances or conductance-induced distances.

Alignment with Performance. We first ask: does a similarity proxy preserve the true structure of transferability? If two tasks are highly related from a model’s perspective, the performance gap between them should be small (Wang et al., 2019). A useful proxy should therefore assign smaller distances to task pairs with smaller performance gaps. To probe this, we select five representative VLMs spanning ResNet and ViT backbones with diverse pretraining sources and compute a task–task proxy matrix using: (i) our conductance representation derived from a 25-image unlabeled set, and (ii) a semantic baseline derived from task text embeddings. Figure 1 illustrates these matrices and the corresponding performance gaps, with further details deferred to Appendix B. While absolute correlations are modest, as expected under extreme supervision constraints, the conductance proxy consistently aligns more closely with ground truth than the semantic baseline.

Table 1. Alignment with Performance Gap. Our method (ρ_{cond}) consistently improves over semantic proxies (ρ_{sem}), especially for ResNets where semantic correlation can be negative.

Model	ρ_{cond} (Ours)	ρ_{sem}	Δ
RN101-OpenAI	0.128	-0.127	+0.255
RN50x4-OpenAI	0.131	-0.095	+0.227
ViT-B/32-OpenAI	0.011	-0.051	+0.062
RN50-CC12M	0.023	0.002	+0.020
ViT-B/16-DFN2B	0.031	0.026	+0.006

Table 1 quantifies this effect via Spearman correlation between the proxy-derived rankings and the performance gap ordering. Notably, for ResNet-based models (RN101-OpenAI and RN50x4-OpenAI), the semantic proxy can even become negatively correlated with ground truth, suggesting that text-only descriptors may invert the transferability signal under certain architectures. In contrast, the conductance proxy remains positively correlated across all five models, confirming its reliability as a selection signal.

The Model-Specific Nature of Task Perception. A second hypothesis central to our method is that task relatedness is model-specific: two tasks perceived as similar by one model may be distinct to another due to differences in architecture, pretraining objectives, and learned features (Achille et al., 2019; Mehra et al., 2024). If true, the task perception induced by conductance should vary across models. To test this, we compare conductance-induced task distance vectors. Figure 2 reports the resulting model-to-model correlation matrix. We observe clear architectural clustering: models within the same backbone family exhibit stronger agreement in relative task distances, while cross-architecture agreement drops substantially. This divergence validates the potential of layer conductance to capture model-specific task perception, motivating our model-specific formulation in Section 4, where target-conditioned importance and directional divergence are computed individually for each candidate model.

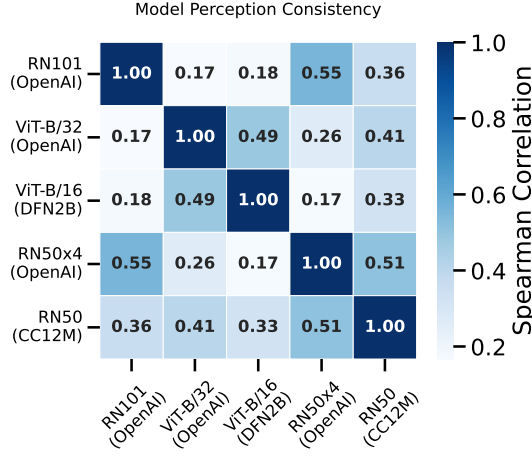


Figure 2. Model-to-Model Correlation Matrix in Task Perception. High correlations within architectural families and low correlations across them indicate model-specific task relationships.

4. Model Selection Via Unlabeled Image

Inspired by the insights of Section 3, this section designs a method to select appropriate VLMs for downstream tasks utilizing a few unlabeled images from the target task.

4.1. Preliminary

The Model. Let \mathcal{M} be a finite set of candidate VLMs and \mathcal{T} a set of downstream tasks. For a model $m \in \mathcal{M}$, we decompose its visual encoder into d_m coarse-grained functional blocks (e.g., stages in ResNet or transformer blocks in ViT), indexed by $i \in \{1, \dots, d_m\}$. The number of blocks d_m may vary across models. Each task $\tau \in \mathcal{T}$, is associated with a small unlabeled image set $\mathcal{X}_\tau = \{x_j\}_{j=1}^{N_\tau}$ sampled i.i.d. from its data distribution P_τ . In the leave-one-out protocol, the held-out target task τ provides N_{tgt} unlabeled images, while each source task $\sigma \in \mathcal{T} \setminus \tau$ provides N_{src} images for constructing task representations (Eq. 4).

Layer Conductance Vector. To quantify the contribution of each block to the model output, we adopt *layer conductance* (Dhamdhere et al., 2019). Given an input image $x \sim P_\tau$ for task $\tau \in \mathcal{T}$, we define the layer conductance vector $g_m(x) \in \mathbb{R}^{d_m}$ as the concatenation of block-wise attribution scores:

$$g_m(x) = \left[g_m^{(1)}(x), \dots, g_m^{(d_m)}(x) \right]^\top. \quad (1)$$

Layer conductance requires a scalar objective. Let $f_m(x) \in \mathbb{R}^p$ denote the visual embedding produced by model m ; in the unlabeled setting, we use the ℓ_2 norm of the image embedding as a representation-strength objective (Xu et al., 2019)

$$F_m(x) \triangleq \|f_m(x)\|_2. \quad (2)$$

This choice is label-free and architecture-agnostic, and aggregates information across embedding dimensions without requiring text prompts or class semantics. In practice, LayerConductance produces an attribution tensor for each block output; we summarize it by the mean absolute attribution over activation dimensions to obtain a scalar score $g_m^{(i)}(x) \in \mathbb{R}_{\geq 0}$. The resulting $g_m(x)$ maps x into a model-specific layer contribution space. More details are in Appendix A. Note that F_m is used only as an unsupervised scalar to extract relative block-importance patterns, rather than as a direct proxy for downstream accuracy.

Task Representation. Since a task is characterized by its underlying distribution rather than individual samples, we define the task representation $v_{m,\tau}$ as the expectation of the conductance vector over P_τ :

$$v_{m,\tau} \triangleq \mathbb{E}_{x \sim P_\tau} [g_m(x)] \in \mathbb{R}^{d_m}. \quad (3)$$

Since P_τ is inaccessible in practice, we approximate $v_{m,\tau}$ by an empirical estimate $\hat{v}_{m,\tau}$ computed from a finite unlabeled sample set $\mathcal{X}_\tau = \{x_j\}_{j=1}^N$ drawn i.i.d. from P_τ :

$$\hat{v}_{m,\tau} \triangleq \frac{1}{N} \sum_{j=1}^N g_m(x_j). \quad (4)$$

N denotes the number of available unlabeled images for task τ , which equals N_{src} for source tasks and N_{tgt} for the held-out target task.

This vector captures the layer-wise dependency structure of task τ on the internal blocks of model m , and serves as the foundation for the subsequent similarity analysis. For notational convenience, we use $v_{m,\tau}^{(i)}$ to denote the i -th component of $v_{m,\tau}$.

4.2. Target-Conditioned Importance Distribution

Given the task representation $v_{m,\tau}$, we aim to identify which blocks are most critical for the target task τ . Treating all blocks uniformly neglects the hierarchical structure of deep networks, where different blocks capture features of varying semantic complexity. We therefore seek an importance distribution $\alpha_{m,\tau} \in \Delta^{d_m-1}$ over the d_m blocks that emphasizes the most relevant blocks while preserving robustness.

Normalization. To eliminate scale variations across models and ensure numerical stability, we define the normalized representation $u_{m,\tau} \in \mathbb{R}^{d_m}$ as:

$$u_{m,\tau} \triangleq \frac{v_{m,\tau}}{\max(\|v_{m,\tau}\|_2, \epsilon)}, \quad (5)$$

where $\epsilon > 0$ is a small constant for numerical stability. Each component $u_{m,\tau}^{(i)}$ reflects the relative contribution of block i to task τ .

Derivation via Entropy-Regularized Alignment. We require the importance distribution $\alpha_{m,\tau}$ to satisfy two desiderata: (I) higher weights for blocks with larger normalized conductance values (alignment), and (II) sufficient dispersion to avoid over-reliance on any single block (robustness).

Following these principles, we define $\alpha_{m,\tau}$ as the solution to an entropy-regularized alignment objective. Specifically, we seek $\alpha \in \Delta^{d_m-1}$ that maximizes a trade-off between alignment with $u_{m,\tau}$ and Shannon entropy $H(\alpha) = -\sum_i \alpha_i \log \alpha_i$:

$$\alpha_{m,\tau} = \arg \max_{\alpha \in \Delta^{d_m-1}} \left(\langle \alpha, u_{m,\tau} \rangle + \frac{1}{\eta} H(\alpha) \right), \quad (6)$$

where $\eta > 0$ is a temperature parameter controlling distribution sharpness.

This objective admits a closed-form solution given by the softmax function, which can be easily verified (see Appendix C for a detailed derivation):

$$\alpha_{m,\tau}^{(i)} = \frac{\exp(\eta u_{m,\tau}^{(i)})}{\sum_{j=1}^{d_m} \exp(\eta u_{m,\tau}^{(j)})}. \quad (7)$$

The resulting distribution depends solely on the target task representation $v_{m,\tau}$ and re-weights blocks according to task demands. The parameter η modulates the degree of concentration: large η focuses mass on dominant blocks, while small η yields a smoother weighting.

4.3. Directional Conductance Divergence

We define a metric to quantify the transferability from a source task σ to the target task τ . Unlike conventional symmetric metrics (e.g., Euclidean or Cosine distance), effective transfer learning hinges on directional coverage (Zamir et al., 2019): a source task is valuable primarily if it encompasses the internal mechanisms critical to the target.

To capture this asymmetry, we propose Directional Conductance Divergence (DCD). We first define the element-wise relative deviation of the source task σ with respect to the target τ at block i :

$$\delta_m^{(i)}(\tau, \sigma) \triangleq \frac{\left| v_{m,\tau}^{(i)} - v_{m,\sigma}^{(i)} \right|}{\left| v_{m,\tau}^{(i)} \right| + \epsilon}, \quad (8)$$

where $\epsilon > 0$ is a small constant for numerical stability. The denominator normalizes by the target activation magnitude, so the divergence is interpreted as a relative error measured in the target’s context.

We then define DCD as the expected relative deviation under

the target’s importance distribution:

$$D_m(\tau \rightarrow \sigma) \triangleq \sum_{i=1}^{d_m} \alpha_{m,\tau}^{(i)} \cdot \delta_m^{(i)}(\tau, \sigma) = \mathbb{E}_{i \sim \alpha_{m,\tau}} [\delta_m^{(i)}(\tau, \sigma)]$$

Intuitively, $D_m(\tau \rightarrow \sigma)$ measures how well the source task σ covers the target-critical mechanisms emphasized by $\alpha_{m,\tau}$: smaller values indicate better coverage.

From Divergence to Similarity The DCD $D_m(\tau \rightarrow \sigma)$ is a nonnegative, target-conditioned divergence. To aggregate evidence across multiple candidate sources, we convert DCD values into a normalized similarity distribution over the source-task set.

Let $\mathcal{S}_\tau \subseteq \mathcal{T} \setminus \{\tau\}$ denote the set of available source tasks for target τ . For a fixed model m , we define a softmin-based similarity score:

$$s_m(\sigma | \tau) \triangleq e^{-\gamma(D_m(\tau \rightarrow \sigma) - \min_{\sigma' \in \mathcal{S}_\tau} D_m(\tau \rightarrow \sigma'))} \quad (9)$$

where $\gamma > 0$ is a temperature parameter modulating the sharpness of the distribution. Subtracting the minimum DCD provides a numerically stable baseline shift without changing the relative ordering across σ .

We normalize the similarity scores to obtain a probability distribution over source tasks:

$$p_m(\sigma | \tau) \triangleq \frac{s_m(\sigma | \tau)}{\sum_{\sigma' \in \mathcal{S}_\tau} s_m(\sigma' | \tau)} \quad (10)$$

Thus, $p_m(\sigma | \tau)$ assigns larger mass to source tasks with smaller DCD, and the distribution becomes more concentrated as γ increases.

Ranking via Similarity Aggregation Given the DCD-induced weights $\{p_m(\sigma | \tau)\}_{\sigma \in \mathcal{S}_\tau}$, we estimate how model m would rank on the target task τ without direct evaluation.

Assume that for each model m and source task $\sigma \in \mathcal{S}_\tau$, we have access to its performance-based rank $R_m(\sigma)$ among all candidate models (smaller is better). That is, $R_m(\sigma)$ is obtained by sorting models by their ground-truth performance on σ and taking the resulting rank value. We then predict the target-task rank of model m via a similarity-weighted average of source-task ranks:

$$\hat{R}_m(\tau) \triangleq \sum_{\sigma \in \mathcal{S}_\tau} p_m(\sigma | \tau) \cdot R_m(\sigma) \quad (11)$$

Finally, given a candidate model set \mathcal{M} , we obtain the estimated ranking for target task τ by sorting models in ascending order of $\hat{R}_m(\tau)$ (smaller is better):

$$\hat{\pi}_\tau \triangleq \text{argsort}_{m \in \mathcal{M}} \hat{R}_m(\tau) \quad (12)$$

This ranking serves as the basis for model selection and is evaluated against ground-truth rankings in our experiments.

5. Theoretical Analysis

Our method adopts model-specific task representations and a directional transfer distance, contrasting with prior symmetric approaches (Zohar et al., 2023; Yi et al., 2024). This section provides theoretical Analysis for the necessity of asymmetry under a coverage-based view of transfer, and explains why our Directional Conductance Divergence (DCD) can be interpreted as a smooth relaxation of an idealized set-restricted formulation.

Definition 5.1 (Salient Set). *Let $\mathbf{u}_{m,\tau} \in \mathbb{R}^{d_m}$ be the normalized representation of task τ on model m . Let $\rho_k(\mathbf{u}_{m,\tau})$ denote the k -th largest value in $\mathbf{u}_{m,\tau}$. The salient set of task τ is defined as*

$$\mathcal{S}_{m,\tau}^{(k)} \triangleq \left\{ i \in \{1, \dots, d_m\} \mid u_{m,\tau}^{(i)} \geq \rho_k(\mathbf{u}_{m,\tau}) \right\}. \quad (13)$$

This set represents the top- k functional blocks on which task τ relies most heavily; for an appropriate choice of k , it serves as a proxy for the task-critical blocks.

Coverage Semantics for Model Selection. We argue that transfer distance from a source task σ to a target task τ should follow *coverage semantics*. If the source activates all target-critical functional blocks (i.e., $\mathcal{S}_{m,\sigma}^{(k)} \supseteq \mathcal{S}_{m,\tau}^{(k)}$), then the transfer distance $d(\tau \rightarrow \sigma)$ should be small. Importantly, additional active blocks in the source that are irrelevant to the target should not be heavily penalized. We formalize this principle via two assumptions on a directional distance function $d(\cdot \rightarrow \cdot)$.

Assumption 5.2 (Target-Sufficiency). *If the source task σ matches the target task τ on all indices in the target salient set, the distance should be zero regardless of discrepancies outside the salient set:*

$$\forall i \in \mathcal{S}_{m,\tau}^{(k)}, \quad u_{m,\sigma}^{(i)} = u_{m,\tau}^{(i)} \implies d(\tau \rightarrow \sigma) = 0.$$

Assumption 5.3 (Salient-Discriminativity). *Conversely, if the source task σ relies on certain salient blocks that the target task τ does not match (when the direction is reversed), the distance must be strictly positive:*

$$\exists j \in \mathcal{S}_{m,\sigma}^{(k)} \text{ s.t. } u_{m,\tau}^{(j)} \neq u_{m,\sigma}^{(j)} \implies d(\sigma \rightarrow \tau) > 0.$$

Proposition 5.4 (Impossibility of Symmetry). *Let $d(\cdot \rightarrow \cdot)$ satisfy Assumptions 5.2 and 5.3. Suppose $\mathcal{S}_{m,\tau}^{(k)} \subsetneq \mathcal{S}_{m,\sigma}^{(k)}$, and the representations match on $\mathcal{S}_{m,\tau}^{(k)}$ but differ on the residual indices $\mathcal{S}_{m,\sigma}^{(k)} \setminus \mathcal{S}_{m,\tau}^{(k)}$. Then d is necessarily asymmetric. The proof is provided in Appendix D.1.*

Remark 5.5. *Proposition 5.4 reveals a limitation of symmetric metrics (e.g., cosine similarity and Euclidean distance) under coverage semantics: they penalize a source for possessing additional capabilities irrelevant to the target, thereby overestimating transfer distances to more comprehensive sources.*

DCD as a Continuous Relaxation (Summary). An ideal coverage-based distance can be defined by restricting attention to the target salient set $\mathcal{S}_{m,\tau}^{(k)}$, but it requires choosing a discrete k for each target task. Our DCD replaces this hard set restriction with the target-conditioned soft weights $\alpha_{m,\tau}$, yielding a smooth, k -free relaxation. Formally, DCD can be decomposed into a set-restricted divergence term plus a residual tail term, and the approximation error is controlled by the tail mass of $\alpha_{m,\tau}$ outside the salient set. The full construction and bounds are deferred to Appendix D.2.

6. Experiments

6.1. Experimental Setup

Datasets and Model Zoo. Building upon the protocols established in the LOVM benchmark (Zohar et al., 2023) and the expansion strategies adopted by SWAB (Yi et al., 2024), we establish our experimental setup using their publicly available datasets and model repositories. To facilitate a more comprehensive evaluation, we augment the original model zoo with additional representative architectures, including EVA01-g-14 (Sun et al., 2023) and nlhb-clip-base (Visheratin, 2023), to expand the collection to a total of 48 models. This extensive model zoo encapsulates a broad spectrum of architectural designs, pre-training corpora, and training paradigms. Detailed information on the datasets and models is provided in Appendix E.

Evaluation Protocol. To ensure a rigorous and equitable comparison, we adhere to the leave-one-out evaluation protocol employed by ModelGPT and SWAB (Yi et al., 2024; Zohar et al., 2023). Specifically, we iteratively designate one of the 21 datasets as the *held-out* target domain, while the remaining datasets constitute the source pool. All datasets are obtained from official repositories and evaluated using standard test splits.

To establish ground-truth rankings, we leverage the text templates provided by LOVM (Zohar et al., 2023) to construct zero-shot classifiers and measure the Top-1 accuracy of each VLM on the respective test splits. To guarantee statistical robustness, we perform 10 independent runs with varying random seeds, reporting the mean and standard deviation for all learning-based methods.

Metrics. To provide a precise assessment of model selection performance, we employ Top-5 NDCG (Normalized Discounted Cumulative Gain) (Järvelin & Kekäläinen, 2017), which offers greater discriminative power compared to the Top-5 Recall metric used in prior studies. Additionally, we report Kendall’s Tau on the top-5 models ($\tau@5$) to ensure comparability. To evaluate the overall capability of each method, we report the sum of NDCG and $\tau@5$. All metrics are better when larger.

6.2. Main Performance Comparison

Baselines. We benchmark our method against several representative baselines from the model selection literature. Specifically, we consider two ranking-based approaches: INB, which ranks VLMs based on their ImageNet performance, and Avg Rank, which calculates the mean rank across all 21 datasets. Furthermore, we compare our approach with two learning-based baselines: ModelGPT (Zohar et al., 2023) and SWAB (Yi et al., 2024), the current state-of-the-art method.

Table 2. Main results on few-shot VLM selection. NDCG@5 and $\tau@5$ are averaged over 10 random seeds for methods (ModelGPT, SWAB, and Ours). Our method is evaluated in the lightweight regime with $N_{tgt}=1$ target image and $N_{src}=25$ source images per task, which attains the best performance in our sampling study. The corresponding distribution over 10 Runs are provided in Appendix F.1. Best in **bold**, second-best underlined.

Metric	INB	AvgRank	ModelGPT	SWAB	Ours
NDCG@5 \uparrow	0.539	0.524	0.544	<u>0.616</u>	0.707
$\tau@5 \uparrow$	0.268	0.254	0.267	<u>0.318</u>	0.365
Sum \uparrow	0.807	0.778	0.811	<u>0.934</u>	1.072
<i>Other metrics:</i>					
NDCG@3 \uparrow	0.384	0.386	0.386	<u>0.393</u>	0.402
NDCG@7 \uparrow	0.651	0.699	<u>0.702</u>	0.691	0.752

Results. As shown in Table 2, we make the following observations. (I). Our method consistently outperforms all baselines, achieving an NDCG@5 of 0.707 (a 14.7% improvement over SWAB) and the highest $\tau@5$ (0.365). (II). The performance gap between our method and SWAB reveals the limitation of relying solely on semantic similarity for model selection. By explicitly accounting for differences in model architecture and pre-training, our attribution-based approach more effectively captures model–task alignment. (III). The larger gain in NDCG@5 relative to $\tau@5$ indicates that our method is particularly effective at identifying and ranking the best-matched model at the top position, which is crucial for practical deployment. Taken together, these results suggest that effective VLM selection requires a model-specific characterization of task relevance. By grounding similarity in model-aware attribution signals, our approach achieves more accurate model–task alignment while remaining efficient with minimal samples.

6.3. Hyperparameter Sensitivity

Our method incorporates two key hyperparameters: η (layer attention intensity), which regulates the softmax temperature to weight network blocks based on their conductance, and γ , which scales task similarity to modulate discriminative strength when aggregating rankings from source tasks. We

evaluate the sensitivity of our approach by varying $\eta \in \{1.5, 2.0, 2.5, 3.0, 3.5\}$ and $\gamma \in \{3.0, 3.5, 4.0, 4.5, 5.0\}$. The results are visualized as heatmaps in Figure 3.

The empirical results demonstrate that our method is highly robust to hyperparameter variations. Specifically, varying η from 1.5 to 3.5 yields only marginal fluctuations in NDCG@5, suggesting that task representations remain discriminative provided that informative layers are sufficiently prioritized. Similarly, performance remains stable across the tested range of γ , with $\tau@5$ ranging from 0.222 to 0.381. The configuration of $\eta = 2.0$ and $\gamma = 5.0$ attains the peak $\tau@5$ (0.365), striking an effective balance between layer-wise noise suppression and task discrimination. These findings confirm that our method maintains strong performance across a broad parameter space without the need for exhaustive per-task tuning.

6.4. Ablation Study

Baselines. To verify the effectiveness of our asymmetric similarity formulation, we compare it with two commonly used symmetric alternatives while keeping all other components of the framework unchanged. Specifically, we consider cosine similarity, which measures the normalized inner product between task representation vectors, and a symmetric soft-KL metric implemented as the Jensen–Shannon divergence over softmax-normalized task representations, capturing distributional similarity in a symmetric manner. All baseline methods rely on the same task representations derived from layer-wise conductance; the only difference lies in the choice of the similarity measure.

Results. Table 3 compares different similarity metrics under a unified experimental setting, from which we draw three key observations. (I) Our asymmetric similarity consistently outperforms both symmetric baselines across all evaluation metrics. Compared with the strongest symmetric alternative, it achieves a 10.5% improvement in NDCG@5 (0.707 vs. 0.640) and a 20.8% gain in $\tau@5$ (0.365 vs. 0.302). (II) Cosine similarity and Jensen–Shannon divergence exhibit nearly identical performance (NDCG@5 of 0.639 and 0.640, respectively), suggesting that under symmetric formulations, the choice between geometric and distributional similarity has a negligible impact on overall performance. (III) The pronounced performance advantage further confirms that task similarity, from a model-specific perspective, is inherently asymmetric: the transfer utility of a source task to a target task is not equivalent to the reverse.

6.5. Efficiency of Source Task Sampling

To evaluate data efficiency, we fix $N_{tgt} = 1$ and vary the number of source samples per task (N_{src}) from 1 to 100, averaging over 5 random seeds. As shown in Figure 4, perfor-

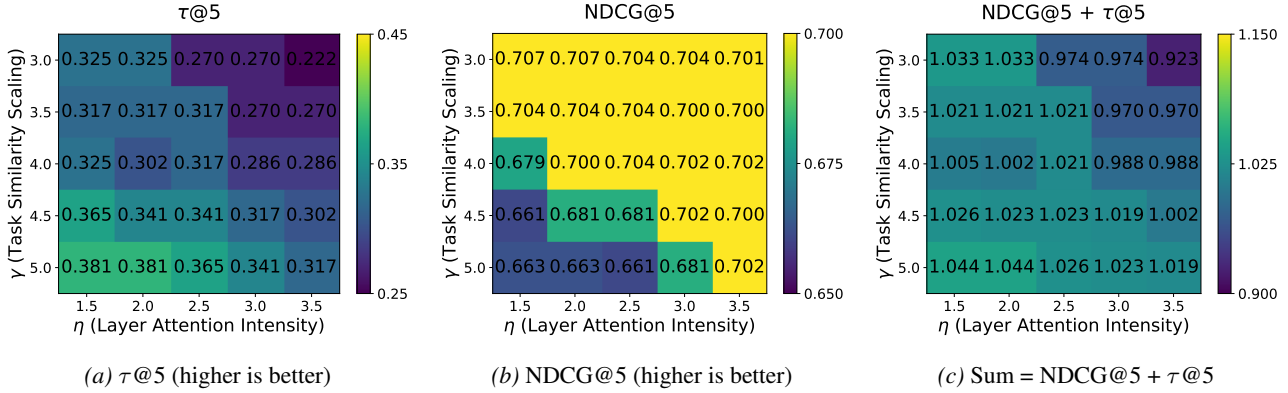


Figure 3. **Sensitivity to η and γ .** Heatmaps of selection performance when varying η (softmax temperature for target-conditioned block importance) and γ (softmax temperature for DCD-based source weighting). All values are averaged over 10 random seeds. Performance is stable across a wide range.

Table 3. **Ablation on similarity metrics.** We keep the conductance-based task representation and the rank aggregation pipeline fixed, and only change the task similarity measure. Our asymmetric DCD consistently outperforms symmetric alternatives.

Metric	NDCG@5 \uparrow	$\tau@5 \uparrow$	Sum \uparrow
Cosine (Sym.)	0.6393	0.3009	0.9402
Soft-KL/JSD (Sym.)	0.6399	0.3016	0.9415
Ours (Asym.)	0.707	0.365	1.072

formance improves rapidly in the low-data regime: NDCG@5 rises from 0.585 to 0.707 and $\tau@5$ reaches 0.365 as N_{src} increases to 25. Beyond this point, metrics saturate around 0.71 (NDCG@5) and 0.38 ($\tau@5$). This confirms that approximately 25 anchor images suffice for robust source task characterization, enabling a lightweight and efficient source library.

7. Conclusion

We introduced a model-specific framework for few-shot vision-language model selection that characterizes tasks through layer-wise contributions in the visual encoder and quantifies transferability using Directional Conductance Divergence (DCD), an asymmetric metric measuring target-critical feature coverage. Empirical evaluation across 48 VLMs and 21 datasets shows significant improvements over existing baselines, achieving NDCG@5 of 0.707 and $\tau@5$ of 0.365, representing gains of approximately 15% over SWAB, while theoretical analysis supports the necessity of asymmetry under coverage semantics.

Future work can improve both the generality and practicality of our framework. We will investigate architecture-aware strategies to align functional blocks across heterogeneous

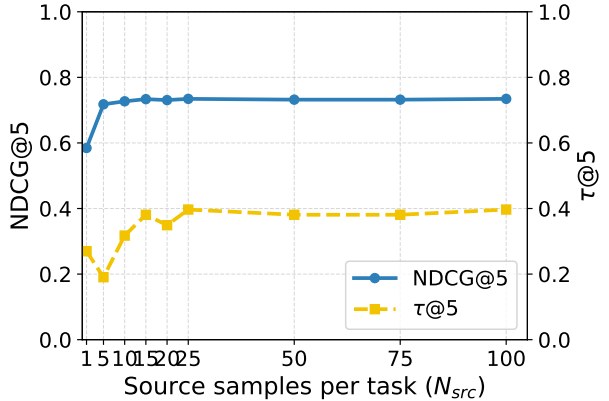


Figure 4. **Impact of Source Task Sample Size (N_{src}).** With a fixed single-shot target representation ($N_{tgt} = 1$), performance improves rapidly and saturates around $N_{src} = 25$, demonstrating that our method requires minimal data to construct the source reference library.

backbones, and extend attribution signals to vision-language interaction for alignment-sensitive tasks. We also plan to strengthen performance under extreme sampling through adaptive anchor selection and uncertainty-aware aggregation. Finally, incorporating robustness and fairness criteria would enable more reliable deployment across diverse scenarios.

References

Achille, A., Lam, M., Tewari, R., Ravichandran, A., Maji, S., Fowlkes, C. C., Soatto, S., and Perona, P. Task2vec: Task embedding for meta-learning. In *Proceedings of the IEEE/CVF International Conference on Computer Vision*, pp. 6429–6438, 2019.

Bao, Y., Li, Y., Huang, S.-L., Zhang, L., Zheng, L., Zamir, A., and Guibas, L. J. An information-theoretic approach to transferability in task transfer learning. In *Proceedings of the IEEE International Conference on Image Processing*, pp. 2309–2313, 2019.

Bau, D., Zhou, B., Khosla, A., Oliva, A., and Torralba, A. Network dissection: Quantifying interpretability of deep visual representations. In *Proceedings of the IEEE Conference on Computer Vision and Pattern Recognition*, pp. 3319–3327, 2017.

Cheng, G., Han, J., and Lu, X. Remote sensing image scene classification: Benchmark and state of the art. *Proceedings of the IEEE*, 105(10):1865–1883, 2017.

Cimpoi, M., Maji, S., Kokkinos, I., Mohamed, S., and Vedaldi, A. Describing textures in the wild. In *Proceedings of the IEEE Conference on Computer Vision and Pattern Recognition*, pp. 3606–3613, 2014.

Coates, A., Ng, A., and Lee, H. An analysis of single-layer networks in unsupervised feature learning. In *Proceedings of the International Conference on Artificial Intelligence and Statistics*, pp. 215–223, 2011.

Cuturi, M. Sinkhorn distances: Lightspeed computation of optimal transport. In *Advances in Neural Information Processing Systems*, pp. 2292–2300, 2013.

Dhamdhere, K., Sundararajan, M., and Yan, Q. How important is a neuron. In *International Conference on Learning Representations*, 2019.

Ding, Y., Jiang, B., Yu, A., Zheng, A., and Liang, J. Which model to transfer? A survey on transferability estimation, 2024.

Dugas, E., Cukierski, W., et al. Diabetic retinopathy detection. Kaggle Competition, 2015. URL <https://kaggle.com/competitions/diabetic-retinopathy-detection>.

Everingham, M., van Gool, L., Williams, C. K. I., Winn, J., and Zisserman, A. The PASCAL visual object classes (VOC) challenge. *International Journal of Computer Vision*, 88(2):303–338, 2010.

Geiger, A., Lenz, P., Stiller, C., and Urtasun, R. Vision meets robotics: The KITTI dataset. *International Journal of Robotics Research*, 32(11):1231–1237, 2013.

Goodfellow, I. J., Erhan, D., Carrier, P.-L., Courville, A., Mirza, M., Hamner, B., Cukierski, W., Tang, Y., Thaler, D., Lee, D.-H., et al. Challenges in representation learning: A report on three machine learning contests. In *International Conference on Neural Information Processing*, pp. 117–124, 2013.

Helber, P., Bischke, B., Dengel, A., and Borth, D. EuroSAT: A novel dataset and deep learning benchmark for land use and land cover classification. *IEEE Journal of Selected Topics in Applied Earth Observations and Remote Sensing*, 12(7):2217–2226, 2019.

Ilharco, G., Wortsman, M., Wightman, R., Gordon, C., Carlini, N., Taori, R., Dave, A., Shankar, V., Namkoong, H., Miller, J., Hajishirzi, H., Farhadi, A., and Schmidt, L. Openclip. Zenodo, 2021.

Järvelin, K. and Kekäläinen, J. IR evaluation methods for retrieving highly relevant documents. *SIGIR Forum*, 51(2):243–250, 2017.

Jia, C., Yang, Y., Xia, Y., Chen, Y.-T., Parekh, Z., Pham, H., Le, Q. V., Sung, Y.-H., Li, Z., and Duerig, T. Scaling up visual and vision-language representation learning with noisy text supervision. In *Proceedings of the International Conference on Machine Learning*, pp. 4904–4916, 2021.

Johnson, J., Hariharan, B., van der Maaten, L., Fei-Fei, L., Zitnick, C. L., and Girshick, R. CLEVR: A diagnostic dataset for compositional language and elementary visual reasoning. In *Proceedings of the IEEE Conference on Computer Vision and Pattern Recognition*, pp. 2901–2910, 2017.

Krause, J., Stark, M., Deng, J., and Fei-Fei, L. 3d object representations for fine-grained categorization. In *Proceedings of the IEEE International Conference on Computer Vision Workshops*, pp. 554–561, 2013.

Krizhevsky, A. and Hinton, G. Learning multiple layers of features from tiny images, 2009.

LeCun, Y., Bottou, L., Bengio, Y., and Haffner, P. Gradient-based learning applied to document recognition. *Proceedings of the IEEE*, 86(11):2278–2324, 2002.

Ma, Y., Song, Z., Zhuang, Y., Hao, J., and King, I. A survey on vision-language-action models for embodied AI, 2024.

Mehra, A., Zhang, Y., and Hamm, J. Understanding the transferability of representations via task-relatedness. In *Advances in Neural Information Processing Systems*, 2024.

Netzer, Y., Wang, T., Coates, A., Bissacco, A., Wu, B., Ng, A. Y., et al. Reading digits in natural images with unsupervised feature learning. NIPS Workshop, 2011.

Nguyen, C. V., Hassner, T., Seeger, M. W., and Archambeau, C. LEEP: A new measure to evaluate transferability of learned representations. In *Proceedings of the International Conference on Machine Learning*, pp. 7294–7305, 2020.

Nilsback, M.-E. and Zisserman, A. Automated flower classification over a large number of classes. In *Proceedings of the Indian Conference on Computer Vision, Graphics & Image Processing*, pp. 722–729, 2008.

Parkhi, O. M., Vedaldi, A., Zisserman, A., and Jawahar, C. V. Cats and dogs. In *Proceedings of the IEEE Conference on Computer Vision and Pattern Recognition*, pp. 3498–3505, 2012.

Radford, A., Kim, J. W., Hallacy, C., Ramesh, A., Goh, G., Agarwal, S., Sastry, G., Askell, A., Mishkin, P., Clark, J., Krueger, G., and Sutskever, I. Learning transferable visual models from natural language supervision. In *Proceedings of the International Conference on Machine Learning*, pp. 8748–8763, 2021.

Sachdeva, B., Uppal, K., Java, A., and Balasubramanian, V. N. Understanding task transfer in vision-language models, 2025.

Schuhmann, C., Beaumont, R., Vencu, R., Gordon, C., Wightman, R., Cherti, M., Coombes, T., Katta, A., Mullis, C., Wortsman, M., Schramowski, P., Kundurthy, S., Crownson, K., Schmidt, L., Kaczmarsky, R., and Jitsev, J. LAION-5b: An open large-scale dataset for training next generation image-text models. In *Advances in Neural Information Processing Systems*, 2022.

Singh, A., Hu, R., Goswami, V., Couairon, G., Galuba, W., Rohrbach, M., and Kiela, D. FLAVA: A foundational language and vision alignment model. In *Proceedings of the IEEE/CVF Conference on Computer Vision and Pattern Recognition*, pp. 15617–15629, 2022.

Stallkamp, J., Schlipsing, M., Salmen, J., and Igel, C. The german traffic sign recognition benchmark: A multi-class classification competition. In *Proceedings of the International Joint Conference on Neural Networks*, pp. 1453–1460, 2011.

Sun, Q., Fang, Y., Wu, L., Wang, X., and Cao, Y. EVA-CLIP: Improved training techniques for CLIP at scale, 2023.

Sun, X., Hou, Y., Deng, W., Li, H., and Zheng, L. Ranking models in unlabeled new environments. In *Proceedings of the IEEE/CVF International Conference on Computer Vision*, pp. 11741–11751, 2021.

Sundararajan, M., Taly, A., and Yan, Q. Axiomatic attribution for deep networks. In *Proceedings of the International Conference on Machine Learning*, pp. 3319–3328, 2017.

Tan, H.-Z., Zhou, Z., Li, Y., and Guo, L.-Z. Vision-language model selection and reuse for downstream adaptation. In *Proceedings of the International Conference on Machine Learning*, 2025.

Veeling, B. S., Linmans, J., Winkens, J., Cohen, T., and Welling, M. Rotation equivariant CNNs for digital pathology. In *International Conference on Medical Image Computing and Computer-Assisted Intervention*, pp. 210–218, 2018.

Visheratin, A. A. NLLB-CLIP: Train performant multilingual image retrieval model on a budget, 2023.

Wang, B., Mendez, J. A., Cai, M., and Eaton, E. Transfer learning via minimizing the performance gap between domains. In *Advances in Neural Information Processing Systems*, pp. 10644–10654, 2019.

Wolf, T., Debut, L., Sanh, V., Chaumond, J., Delangue, C., Moi, A., Cistac, P., Rault, T., Louf, R., Funtowicz, M., Davison, J., Shleifer, S., von Platen, P., Ma, C., Jernite, Y., Plu, J., Xu, C., Le Scao, T., Gugger, S., Drame, M., Lhoest, Q., and Rush, A. M. Transformers: State-of-the-art natural language processing. In *Proceedings of the Conference on Empirical Methods in Natural Language Processing: System Demonstrations*, pp. 38–45, 2020.

Xiao, J., Hays, J., Ehinger, K. A., Oliva, A., and Torralba, A. SUN database: Large-scale scene recognition from abbey to zoo. In *Proceedings of the IEEE Conference on Computer Vision and Pattern Recognition*, pp. 3485–3492, 2010.

Xu, R., Li, G., Yang, J., and Lin, L. Larger norm more transferable: An adaptive feature norm approach for unsupervised domain adaptation. In *Proceedings of the IEEE/CVF International Conference on Computer Vision*, pp. 1426–1435, 2019.

Xue, Y., Yang, R., Chen, X., Liu, W., Wang, Z., and Liu, X. A review on transferability estimation in deep transfer learning. *IEEE Transactions on Artificial Intelligence*, 5 (12):5894–5914, 2024.

Yang, S., Zhai, B., You, Q., Yuan, J., Yang, H., and Xu, C. Law of vision representation in MLLMs, 2024.

Yi, C., He, Y., Zhan, D.-C., and Ye, H.-J. Bridge the modality and capability gaps in vision-language model selection. In *Advances in Neural Information Processing Systems*, 2024.

You, K., Liu, Y., Wang, J., and Long, M. LogME: Practical assessment of pre-trained models for transfer learning. In *Proceedings of the International Conference on Machine Learning*, pp. 12133–12143, 2021.

Yu, J., Wang, Z., Vasudevan, V., Yeung, L., Seyedhosseini, M., and Wu, Y. CoCa: Contrastive captioners are image-text foundation models. *Transactions on Machine Learning Research*, 2022.

Yuan, L. et al. Florence: A new foundation model for computer vision, 2021.

Zamir, A., Sax, A., Shen, W. B., Guibas, L. J., Malik, J., and Savarese, S. Taskonomy: Disentangling task transfer learning. In *Proceedings of the International Joint Conference on Artificial Intelligence*, pp. 6241–6245, 2019.

Zeiler, M. D. and Fergus, R. Visualizing and understanding convolutional networks. In *European Conference on Computer Vision*, pp. 818–833, 2014.

Zhai, X., Puigcerver, J., Kolesnikov, A., Ruyssen, P., Riquelme, C., Lucic, M., Djolonga, J., Pinto, A. S., Neumann, M., Dosovitskiy, A., et al. A large-scale study of representation learning with the visual task adaptation benchmark, 2019.

Zhang, J., Huang, J., Jin, S., and Lu, S. Vision-language models for vision tasks: A survey. *IEEE Transactions on Pattern Analysis and Machine Intelligence*, 46(8):5625–5644, 2024.

Zhang, Y.-K., Huang, T.-J., Ding, Y.-X., Zhan, D.-C., and Ye, H.-J. Model spider: Learning to rank pre-trained models efficiently. In *Advances in Neural Information Processing Systems*, 2023.

Zohar, O., Huang, S.-C., Wang, K.-C., and Yeung, S. LOVM: Language-only vision model selection. In *Advances in Neural Information Processing Systems*, 2023.

A. Layer Conductance’s Detail

Intuition. Layer conductance quantifies the contribution of individual neurons to the final prediction by measuring the flow of attribution through them. A neuron with high conductance acts as a critical hub linking input features to the model output, indicating its pivotal role in the decision-making process.

Background and notation. Let $F : \mathbb{R}^n \rightarrow \mathbb{R}$ denote the scalar model output used for attribution, with input $x \in \mathbb{R}^n$ and baseline $x' \in \mathbb{R}^n$. We consider the straight-line path $\gamma(\alpha) = x' + \alpha(x - x')$ for $\alpha \in [0, 1]$.

Scalar objective used in this paper. For a VLM m , let $f_m(x) \in \mathbb{R}^p$ be its image embedding. We define

$$F_m(x) \triangleq \|f_m(x)\|_2, \quad (14)$$

and compute layer conductance with respect to $F_m(x)$. This provides a label-free scalar objective that does not require text prompts and aggregates attribution across embedding dimensions. Unless otherwise specified, we use the default settings in Captum.

Integrated Gradients. Integrated Gradients (IG) attributes the prediction to input features. For the i -th feature,

$$\text{IG}_i(x) := (x_i - x'_i) \int_0^1 \frac{\partial F(\gamma(\alpha))}{\partial x_i} d\alpha. \quad (15)$$

Layer conductance formulation. For a hidden neuron y (scalar activation), layer conductance extends IG by decomposing attribution flow through y . The conductance of y with respect to input feature i is

$$\text{Cond}_i^y(x) := (x_i - x'_i) \int_0^1 \frac{\partial F(\gamma(\alpha))}{\partial y} \frac{\partial y}{\partial x_i} d\alpha. \quad (16)$$

The total conductance of y aggregates contributions from all inputs:

$$\text{Cond}^y(x) := \sum_i (x_i - x'_i) \int_0^1 \frac{\partial F(\gamma(\alpha))}{\partial y} \frac{\partial y}{\partial x_i} d\alpha. \quad (17)$$

For a layer $h(x) \in \mathbb{R}^m$ with neurons $\{y_j\}_{j=1}^m$, layer conductance returns $\{\text{Cond}^{y_j}(x)\}_{j=1}^m$. It satisfies completeness: $\sum_{j=1}^m \text{Cond}^{y_j}(x) = F(x) - F(x')$.

Efficient computation. Direct evaluation of Eq. 17 requires computing $\frac{\partial y}{\partial x_i}$ for all input dimensions, which is costly. By recognizing the equivalence between total conductance and path integrated gradients on hidden activations, we rewrite

$$\text{Cond}^y(x) = \int_0^1 \frac{\partial F(\gamma(\alpha))}{\partial \gamma_y(\alpha)} \frac{\partial \gamma_y(\alpha)}{\partial \alpha} d\alpha, \quad (18)$$

where $\gamma_y(\alpha) = y(\gamma(\alpha))$ is the activation of y along the path. We approximate the integral via Riemann sum. Let $x^{(k)} = x' + \frac{k}{n}(x - x')$ and $y^{(k)} = y(x^{(k)})$ for $k = 0, \dots, n$. Then

$$\text{Cond}^y(x) \approx \sum_{k=1}^n \frac{\partial F(x^{(k)})}{\partial y^{(k)}} (y^{(k)} - y^{(k-1)}). \quad (19)$$

This formulation avoids computing input-level gradients and scales efficiently to high-dimensional settings.

Block score aggregation. Captum returns a tensor-valued conductance attribution for the chosen block output. We convert it to a scalar block score by taking the mean absolute attribution over all tensor entries:

$$g_m^{(i)}(x) \triangleq \text{Mean}(|\text{Cond}_m^{(i)}(x)|), \quad (20)$$

where $\text{Cond}_m^{(i)}(x)$ denotes the conductance attribution tensor for block i . We then form $g_m(x) = [g_m^{(1)}(x), \dots, g_m^{(d_m)}(x)]^\top$, and compute the task representation by averaging $g_m(x)$ over unlabeled samples.

Implementation. We use PyTorch Captum (captum.attr.LayerConductance), which implements the efficient computation in Eq. 19. For detailed derivations and theoretical properties, see Dhamdhere et al. (2019).

B. Details regarding Section 3

We analyze five representative VLMs (ResNet and ViT backbones; diverse pre-training sources) on the same $|\mathcal{T}|=21$ downstream tasks. For each task τ , we sample $N_{\text{src}}=25$ unlabeled images and compute conductance-based task representations $\hat{v}_{m,\tau}$ following Section 4.1. We use $\eta=2.5$ and $\epsilon=10^{-8}$ throughout.

Performance gap matrix (Fig. 1, left). For each model m , let $a_m(\tau)$ be its benchmark score on task τ (e.g., accuracy; for non-accuracy metrics we use the task’s primary scalar score). We define the ground-truth task-pair performance gap matrix

$$G_m(\tau, \sigma) \triangleq |a_m(\tau) - a_m(\sigma)|. \quad (21)$$

Proxy gap matrix (Fig. 1, right). *Semantic:* we embed each task τ using model m ’s text encoder (averaging normalized text features over class-name prompts ‘A photo of {c}.’) to obtain $e_m(\tau)$, and set

$$G_m^{\text{sem}}(\tau, \sigma) \triangleq 1 - \cos(e_m(\tau), e_m(\sigma)). \quad (22)$$

Conductance: we compute the target-conditioned importance $\alpha_{m,\tau}$ (Section 4.2) and directional divergence (Section 4.3)

$$D_m(\tau \rightarrow \sigma) \triangleq \sum_{i=1}^{d_m} \alpha_{m,\tau}^{(i)} \cdot \frac{|\hat{v}_{m,\tau}^{(i)} - \hat{v}_{m,\sigma}^{(i)}|}{|\hat{v}_{m,\tau}^{(i)}| + \epsilon}, \quad (23)$$

then symmetrize it to match the undirected proxy gap in Fig. 1:

$$G_m^{\text{cond}}(\tau, \sigma) \triangleq \frac{1}{2}(D_m(\tau \rightarrow \sigma) + D_m(\sigma \rightarrow \tau)). \quad (24)$$

Proxy reliability (Table 1). Let $\text{Vec}(\cdot)$ flatten the upper-triangular entries excluding the diagonal (Fig. 1). For each model m , we compute

$$\rho_{\text{cond}}(m) = \text{Spearman}(\text{Vec}(G_m), \text{Vec}(G_m^{\text{cond}})), \quad \rho_{\text{sem}}(m) = \text{Spearman}(\text{Vec}(G_m), \text{Vec}(G_m^{\text{sem}})). \quad (25)$$

Model-specific task perception (Fig. 2). For any two models (m_1, m_2) , we measure agreement in conductance-induced task distances by

$$\text{Corr}(m_1, m_2) = \text{Spearman}(\text{Vec}(G_{m_1}^{\text{cond}}), \text{Vec}(G_{m_2}^{\text{cond}})), \quad (26)$$

and stack $\text{Corr}(m_1, m_2)$ into the model–model correlation matrix.

C. Derivation of Entropy-Regularized Alignment

In this section, we provide the detailed derivation for the closed-form solution of the importance distribution $\alpha_{m,\tau}$. For notational simplicity and without loss of generality, we drop the subscripts (m, τ) and denote the alignment vector as $u \in \mathbb{R}^d$ and the decision variable as $\alpha \in \Delta^{d-1}$.

C.1. Problem Formulation

Consider the entropy-regularized alignment problem:

$$\max_{\alpha \in \Delta^{d-1}} \left\{ \langle \alpha, u \rangle + \frac{1}{\eta} H(\alpha) \right\}, \quad (27)$$

where $\Delta^{d-1} = \{\alpha \in \mathbb{R}^d : \alpha \geq 0, \mathbf{1}^\top \alpha = 1\}$ denotes the $(d-1)$ -dimensional probability simplex, $H(\alpha) = -\sum_i \alpha_i \log \alpha_i$ is the Shannon entropy, and $\eta > 0$ is a temperature parameter.

C.2. Closed-Form Solution

Theorem C.1. *The optimization problem in (27) admits a unique global maximizer α^* , given by:*

$$\alpha^* = \text{softmax}(\eta u), \quad \text{i.e.,} \quad \alpha_i^* = \frac{\exp(\eta u_i)}{\sum_{j=1}^d \exp(\eta u_j)}. \quad (28)$$

Proof. The proof proceeds in three steps.

Step 1: Strict Concavity and Interior Solution. The objective $\mathcal{J}(\alpha)$ is strictly concave over $\text{int}(\Delta^{d-1})$, being the sum of a linear function and the strictly concave entropy $H(\alpha)$. This guarantees uniqueness of the maximizer. Moreover, since $\nabla H(\alpha) \rightarrow -\infty$ as $\alpha_i \rightarrow 0^+$, the optimal solution lies strictly in the simplex interior ($\alpha_i^* > 0$), and the non-negativity constraints are inactive.

Step 2: KKT Conditions. We form the Lagrangian with multiplier λ for the equality constraint:

$$\mathcal{L}(\alpha, \lambda) = \langle \alpha, u \rangle - \frac{1}{\eta} \sum_i \alpha_i \log \alpha_i + \lambda(\mathbf{1}^\top \alpha - 1). \quad (29)$$

The stationarity condition $\nabla_\alpha \mathcal{L} = 0$ yields:

$$u_i - \frac{1}{\eta}(\log \alpha_i + 1) + \lambda = 0, \quad \forall i. \quad (30)$$

Rearranging (30):

$$\log \alpha_i = \eta(u_i + \lambda) - 1 \implies \alpha_i = e^{\eta \lambda - 1} \cdot e^{\eta u_i}. \quad (31)$$

Denoting $C \triangleq e^{\eta \lambda - 1}$, we have $\alpha_i = C \cdot e^{\eta u_i}$.

Step 3: Normalization. Imposing $\mathbf{1}^\top \alpha = 1$:

$$C \sum_{j=1}^d e^{\eta u_j} = 1 \implies C = \left(\sum_{j=1}^d e^{\eta u_j} \right)^{-1}. \quad (32)$$

Substituting back yields (28). Since $\exp(\eta u_i) > 0$ for all i , the solution satisfies $\alpha_i^* > 0$, confirming feasibility. \square

D. Additional Proofs for Section 5

D.1. Proof of Proposition 5.4

Proof. Evaluate the distance in both directions:

- **Forward** ($\tau \rightarrow \sigma$). Since σ matches τ on all indices in $\mathcal{S}_{m,\tau}^{(k)}$, Assumption 5.2 yields $d(\tau \rightarrow \sigma) = 0$.
- **Reverse** ($\sigma \rightarrow \tau$). There exists $j \in \mathcal{S}_{m,\sigma}^{(k)} \setminus \mathcal{S}_{m,\tau}^{(k)}$ where the representations differ. By Assumption 5.3, $d(\sigma \rightarrow \tau) > 0$.

Hence $d(\tau \rightarrow \sigma) \neq d(\sigma \rightarrow \tau)$, so d is asymmetric. \square

D.2. DCD as a Continuous Relaxation

This appendix provides the full construction and bounds deferred from Section 5. First, the coverage semantics in Section 5 can be satisfied by a set-restricted divergence that focuses solely on the target’s salient blocks. Recall that $S_{m,\tau}^{(k)}$ denotes the salient set of task τ (Definition 5.1). Define the tail mass of the importance distribution as

$$t_{m,\tau}^{(k)}(\eta) \triangleq \sum_{i \notin S_{m,\tau}^{(k)}} \alpha_{m,\tau}^{(i)}. \quad (33)$$

The hard importance distribution supported exclusively on $S_{m,\tau}^{(k)}$ is then

$$\bar{\alpha}_{m,\tau}^{(i)}(\eta) \triangleq \begin{cases} \alpha_{m,\tau}^{(i)} / (1 - t_{m,\tau}^{(k)}(\eta)), & i \in S_{m,\tau}^{(k)}, \\ 0, & \text{otherwise,} \end{cases} \quad (34)$$

which yields the *set-coverage divergence*

$$d_m^{(k)}(\tau \rightarrow \sigma; \eta) \triangleq \sum_{i=1}^{d_m} \bar{\alpha}_{m,\tau}^{(i)}(\eta) \delta_m^{(i)}(\tau, \sigma). \quad (35)$$

While $d_m^{(k)}$ exactly captures the coverage semantics, it requires a discrete choice of k for which no principled criterion exists. We therefore adopt DCD $D_m(\tau \rightarrow \sigma)$ as a smooth relaxation, replacing the hard indicator $\mathbf{1}[i \in S_{m,\tau}^{(k)}]$ with softmax weights $\alpha_{m,\tau}$. Then we quantify this relaxation via the tail mass $t_{m,\tau}^{(k)}(\eta)$.

Lemma D.1 (Tail Mass Bound). *Let $\Delta_k \triangleq u_{(k)} - u_{(k+1)}$ be the gap between the k -th and $(k+1)$ -th largest entries of $\mathbf{u}_{m,\tau}$. The tail mass satisfies*

$$t_{m,\tau}^{(k)}(\eta) \leq \frac{d_m - k}{k} \exp(-\eta \Delta_k). \quad (36)$$

Proof. Let $S \triangleq S_{m,\tau}^{(k)}$ and denote $\alpha^{(i)} \triangleq \alpha_{m,\tau}^{(i)}$ for brevity. By definition of softmax,

$$\sum_{i \notin S} \alpha^{(i)} = \sum_{i \notin S} \frac{\exp(\eta u_{m,\tau}^{(i)})}{\sum_{j=1}^{d_m} \exp(\eta u_{m,\tau}^{(j)})} = \frac{\sum_{i \notin S} \exp(\eta u_{m,\tau}^{(i)})}{\sum_{j=1}^{d_m} \exp(\eta u_{m,\tau}^{(j)})}. \quad (37)$$

Lower bound the denominator by keeping only the contribution of indices in S :

$$\sum_{j=1}^{d_m} \exp(\eta u_{m,\tau}^{(j)}) \geq \sum_{j \in S} \exp(\eta u_{m,\tau}^{(j)}). \quad (38)$$

Hence

$$\sum_{i \notin S} \alpha^{(i)} \leq \frac{\sum_{i \notin S} \exp(\eta u_{m,\tau}^{(i)})}{\sum_{j \in S} \exp(\eta u_{m,\tau}^{(j)})}. \quad (39)$$

Let $u_{(1)} \geq \dots \geq u_{(d_m)}$ be the sorted entries of $\mathbf{u}_{m,\tau}$. Under $\Delta_k = u_{(k)} - u_{(k+1)} > 0$, we have $|S| = k$, and for any $i \notin S$, $u_{m,\tau}^{(i)} \leq u_{(k+1)}$, while for any $j \in S$, $u_{m,\tau}^{(j)} \geq u_{(k)}$. Therefore,

$$\sum_{i \notin S} \exp(\eta u_{m,\tau}^{(i)}) \leq (d_m - k) \exp(\eta u_{(k+1)}), \quad \sum_{j \in S} \exp(\eta u_{m,\tau}^{(j)}) \geq k \exp(\eta u_{(k)}). \quad (40)$$

Combining the above inequalities yields

$$\sum_{i \notin S} \alpha^{(i)} \leq \frac{(d_m - k) \exp(\eta u_{(k+1)})}{k \exp(\eta u_{(k)})} = \frac{d_m - k}{k} \exp(-\eta(u_{(k)} - u_{(k+1)})) = \frac{d_m - k}{k} \exp(-\eta \Delta_k). \quad (41)$$

This concludes the proof of Lemma D.1. \square

Proposition D.2 (DCD as a Set-Restricted Relaxation). *There exists $B > 0$ such that $\delta_m^{(i)}(\tau, \sigma) \leq B$ for all i . For any source task σ , the following holds*

$$\begin{aligned} D_m(\tau \rightarrow \sigma) \\ = \left(1 - t_{m,\tau}^{(k)}(\eta)\right) d_m^{(k)}(\tau \rightarrow \sigma; \eta) + r_m^{(k)}(\tau, \sigma; \eta), \end{aligned} \quad (42)$$

where

$$r_m^{(k)}(\tau, \sigma; \eta) \triangleq \sum_{i \notin S_{m,\tau}^{(k)}} \alpha_{m,\tau}^{(i)} \delta_m^{(i)}(\tau, \sigma). \quad (43)$$

Furthermore, the following holds

$$\begin{aligned} 0 &\leq r_m^{(k)}(\tau, \sigma; \eta) \leq B t_{m,\tau}^{(k)}(\eta), \\ |D_m(\tau \rightarrow \sigma) - d_m^{(k)}(\tau \rightarrow \sigma; \eta)| &\leq 2B t_{m,\tau}^{(k)}(\eta). \end{aligned} \quad (44)$$

Consequently, combining with Lemma D.1, $D_m(\tau \rightarrow \sigma)$ approximates the set-restricted coverage divergence $d_m^{(k)}(\tau \rightarrow \sigma; \eta)$ with an $O(\exp(-\eta\Delta_k))$ error.

Proof. Let $S \triangleq \mathcal{S}_{m,\tau}^{(k)}$, $\alpha^{(i)} \triangleq \alpha_{m,\tau}^{(i)}$, and $\delta^{(i)} \triangleq \delta_m^{(i)}(\tau, \sigma)$ for brevity. Define the tail mass $t \triangleq \sum_{i \notin S} \alpha^{(i)}$, so that $\sum_{i \in S} \alpha^{(i)} = 1 - t$. By definition,

$$D_m(\tau \rightarrow \sigma) = \sum_{i=1}^{d_m} \alpha^{(i)} \delta^{(i)} = \sum_{i \in S} \alpha^{(i)} \delta^{(i)} + \sum_{i \notin S} \alpha^{(i)} \delta^{(i)}. \quad (45)$$

Define the hard distribution $\bar{\alpha}^{(i)}$ supported on S by

$$\bar{\alpha}^{(i)} = \begin{cases} \alpha^{(i)} / (1 - t), & i \in S, \\ 0, & i \notin S, \end{cases} \quad (46)$$

and the set-restricted divergence

$$d_m^{(k)}(\tau \rightarrow \sigma; \eta) = \sum_{i=1}^{d_m} \bar{\alpha}^{(i)} \delta^{(i)} = \sum_{i \in S} \frac{\alpha^{(i)}}{1 - t} \delta^{(i)}. \quad (47)$$

Then

$$\sum_{i \in S} \alpha^{(i)} \delta^{(i)} = (1 - t) \sum_{i \in S} \frac{\alpha^{(i)}}{1 - t} \delta^{(i)} = (1 - t) d_m^{(k)}(\tau \rightarrow \sigma; \eta). \quad (48)$$

Let $r_m^{(k)}(\tau, \sigma; \eta) \triangleq \sum_{i \notin S} \alpha^{(i)} \delta^{(i)}$. This gives the claimed decomposition:

$$D_m(\tau \rightarrow \sigma) = (1 - t) d_m^{(k)}(\tau \rightarrow \sigma; \eta) + r_m^{(k)}(\tau, \sigma; \eta). \quad (49)$$

Since each $\alpha^{(i)} \geq 0$ and each $\delta^{(i)} \geq 0$, we have $r_m^{(k)}(\tau, \sigma; \eta) \geq 0$. Under the boundedness assumption $\delta^{(i)} \leq B$ for all i ,

$$r_m^{(k)}(\tau, \sigma; \eta) = \sum_{i \notin S} \alpha^{(i)} \delta^{(i)} \leq \sum_{i \notin S} \alpha^{(i)} \cdot B = Bt, \quad (50)$$

proving $0 \leq r_m^{(k)}(\tau, \sigma; \eta) \leq Bt$. Moreover, since $d_m^{(k)}(\tau \rightarrow \sigma; \eta)$ is an expectation of $\delta^{(i)}$ under a probability distribution supported on S , it also satisfies $0 \leq d_m^{(k)}(\tau \rightarrow \sigma; \eta) \leq B$. Therefore,

$$D_m(\tau \rightarrow \sigma) - d_m^{(k)}(\tau \rightarrow \sigma; \eta) = -t \cdot d_m^{(k)}(\tau \rightarrow \sigma; \eta) + r_m^{(k)}(\tau, \sigma; \eta), \quad (51)$$

and hence

$$|D_m(\tau \rightarrow \sigma) - d_m^{(k)}(\tau \rightarrow \sigma; \eta)| \leq t \cdot B + Bt = 2Bt. \quad (52)$$

Finally, substituting the bound on t from Lemma D.1 yields the stated $O(\exp(-\eta\Delta_k))$ approximation rate. \square

Corollary D.3. *If the source matches the target on the target salient set, i.e., $\delta_m^{(i)}(\tau, \sigma) = 0$ for all $i \in S_{m,\tau}^{(k)}$, then*

$$D_m(\tau \rightarrow \sigma) = r_m^{(k)}(\tau, \sigma; \eta) \leq B t_{m,\tau}^{(k)}(\eta) \leq B \cdot \frac{d_m - k}{k} \exp(-\eta\Delta_k). \quad (53)$$

and hence $D_m(\tau \rightarrow \sigma) \rightarrow 0$ when η or Δ_k is sufficiently large. Thus, DCD recovers the discrete Target-Sufficiency coverage semantics (Assumption 5.2) while remaining intrinsically asymmetric as required by Proposition 5.4, through its target-conditioned weighting $\alpha_{m,\tau}$.

E. Dataset and Model Details

E.1. Model Zoo

We curated a diverse model zoo by extending the collections in LOVM (Zohar et al., 2023) and SWAB (Yi et al., 2024). Incorporating additional architectures like EVA01-g-14 (Sun et al., 2023) and nllb-clip-base (Visheratin, 2023), our final benchmark comprises 48 models, as detailed in Table 4.

Table 4. Overview of the model zoo used in our experiments. The table details the model name, pre-training tag, parameter count, FLOPs, and ImageNet classification accuracy. Most data are sourced from (Tan et al., 2025).

Model (Family)	Pretrain Tag	Params(M)	FLOPs(B)	ImageNet Acc. (%)
RN50	openai	102.01	18.18	59.82
RN50	cc12m	102.01	18.18	35.91
RN101	openai	119.69	25.50	62.28
RN101	yfcc15m	119.69	25.50	34.07
RN101-quickgelu	openai	119.69	25.50	62.28
RN101-quickgelu	yfcc15m	119.69	25.50	34.87
RN50x4	openai	178.30	51.82	66.27
RN50x64	openai	623.26	552.65	73.91
ViT-B-32	openai	151.28	14.78	63.32
ViT-B-32	laion2b_e16	151.28	14.78	65.65
ViT-B-32	datacomp_xl_s13b_b90k	151.28	14.78	69.17
ViT-B-32	commonpool_m_clip_s128m_b4k	151.28	14.78	27.25
ViT-B-32-256	datacomp_s34b_b86k	151.29	17.46	72.81
ViT-B-32-quickgelu	laion400m_e31	151.28	14.78	62.94
ViT-B-32-quickgelu	metaclip_fullcc	151.28	14.78	67.66
ViT-B-16	openai	149.62	41.09	68.34
ViT-B-16	laion2b_s34b_b88k	149.62	41.09	70.23
ViT-B-16	datacomp_l_s1b_b8k	149.62	41.09	63.10
ViT-B-16	commonpool_l_laion_s1b_b8k	149.62	41.09	55.26
ViT-B-16	dfn2b	149.62	41.09	76.24
ViT-B-16-quickgelu	metaclip_fullcc	149.62	41.09	72.12
ViT-B-16-plus-240	laion400m_e31	208.38	64.03	69.04
ViT-L-14	openai	427.62	175.33	75.54
ViT-L-14	laion400m_e31	427.62	175.33	72.71
ViT-L-14	datacomp_xl_s13b_b90k	427.62	175.33	79.21
ViT-L-14	commonpool_xl_clip_s13b_b90k	427.62	175.33	76.37
ViT-L-14-quickgelu	metaclip_fullcc	427.62	175.33	79.17
ViT-L-14-quickgelu	dfn2b	427.62	175.33	81.41
ViT-L-14-336	openai	427.94	395.22	76.56
ViT-H-14	laion2b_s32b_b79k	986.11	381.68	77.96
ViT-H-14-quickgelu	metaclip_fullcc	986.11	381.68	80.51
ViT-H-14-378-quickgelu	dfn5b	986.71	1054.05	84.37
ViT-g-14	laion2b_s12b_b42k	1366.68	581.15	76.63
ViT-bigG-14	laion2b_s39b_b160k	2539.57	1065.36	80.09
roberta-ViT-B-32	laion2b_s12b_b32k	212.72	105.87	61.71
xlm-roberta-base-ViT-B-32	laion5b_s13b_b90k	366.12	105.87	62.36
convnext_base_w	laion2b_s13b_b82k	179.39	49.38	70.78
convnext_base_w_320	laion_aesthetic_s13b_b82k	179.39	71.94	71.67
convnext_large_d	laion2b_s26b_b102k_augreg	351.77	107.50	75.91
convnext_large_d_320	laion2b_s29b_b131k_ft	351.77	157.98	76.60
convnext_xxlarge	laion2b_s34b_b82k_augreg_soup	1200.58	443.03	79.47
coca_ViT-B-32	laion2b_s13b_b90k	253.56	33.34	63.31
coca_ViT-L-14	laion2b_s13b_b90k	638.45	214.52	75.61
EVA01-g-14	laion400m_s11b_b41k	1136.44	547.36	78.52
EVA02-B-16	merged2b_s8b_b131k	149.69	41.09	74.72
EVA02-L-14-336	merged2b_s6b_b61k	428.08	395.16	80.39

Continued on next page.

Model	Pretrain Tag	Params(M)	FLOPs(B)	ImageNet Acc. (%)
nllb-clip-base	v1	501.89	369.60	24.32
nllb-clip-base-siglip	v1	507.47	472.91	39.09

E.2. Datasets

To evaluate model selection under diverse real-world conditions, we employ datasets spanning various image domains and tasks, as summarized in Table 5.

Table 5. Datasets used in our evaluation, with the corresponding domain type and task. Most data are sourced from (Zohar et al., 2023).

Dataset	Domain	Task
Stanford Cars(Krause et al., 2013)	car picture	image classification
CIFAR100(Krizhevsky & Hinton, 2009)	natural picture	image classification
CLEVR-D(Johnson et al., 2017)	natural picture	object distance estimation
Country211(Radford et al., 2021)	natural picture	geo-localization
Retinopathy(Dugas et al., 2015)	retina scan	image classification
DMLab(Zhai et al., 2019)	natural picture	object distance estimation
DTD(Cimpoi et al., 2014)	texture picture	image classification
EuroSAT(Helber et al., 2019)	satellite images	image classification
FER2013(Goodfellow et al., 2013)	facial picture	facial expression classification
GTSRB(Stallkamp et al., 2011)	traffic picture	image classification
KITTI(Geiger et al., 2013)	nature picture	object distance estimation
MNIST(LeCun et al., 2002)	digit picture	image classification
Flowers102(Nilsback & Zisserman, 2008)	flower picture	image classification
Oxford Pet(Parkhi et al., 2012)	pet photograph	image classification
PCam(Veeling et al., 2018)	medical picture	image classification
RenderedSST2(Radford et al., 2021)	text picture	optical character recognition
RESISC45(Cheng et al., 2017)	satellite picture	land cover classification
STL10(Coates et al., 2011)	natural picture	image classification
SUN397(Xiao et al., 2010)	natural picture	scene classification
SVHN(Netzer et al., 2011)	natural picture	OCR
VOC2007(Everingham et al., 2010)	natural picture	image and pose classification

F. Miscellaneous Details

F.1. Distribution over 10 Runs for Main Results

Figure 5 shows the boxplots of the main results over 10 random runs.

F.2. Evaluation Metrics

For each task τ , we compare estimated ranking $\hat{\pi}_\tau$ (from $\hat{R}_m(\tau)$, Sec. 4.3) against ground-truth π_τ^* (from $R_m(\tau)$) on the Top-k intersection

$$\mathcal{I}_\tau^k \triangleq \{m \mid \hat{r}_\tau(m) \leq k\} \cap \{m \mid r_\tau^*(m) \leq k\}, \quad (54)$$

where $\hat{r}_\tau(m)$ and $r_\tau^*(m)$ denote predicted and ground-truth ranks. We report NDCG@k, Kendall’s τ @k (SciPy implementation with tie-handling), and their sum; both metrics are set to 0 when $|\mathcal{I}_\tau^k| < 2$.

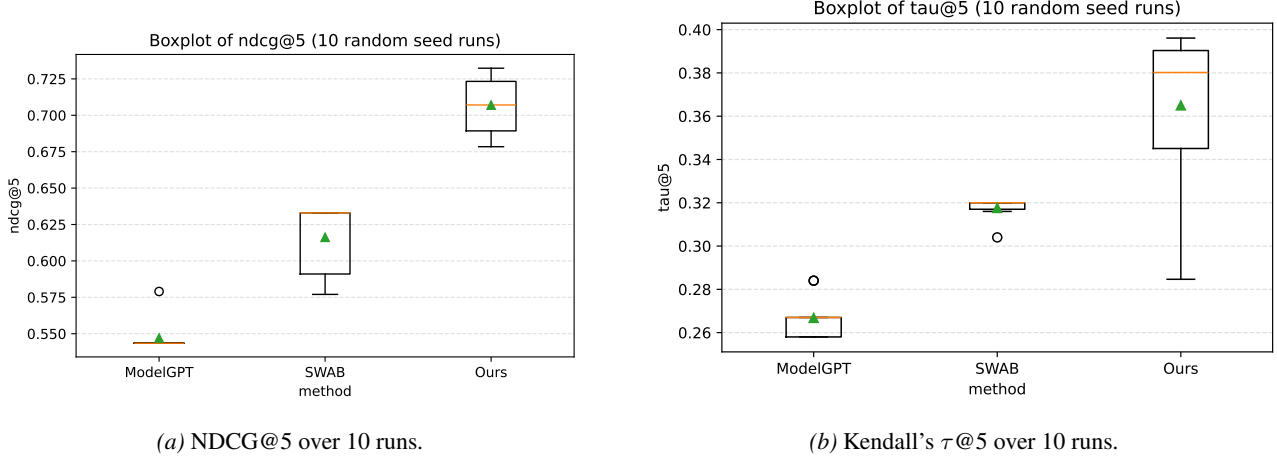


Figure 5. Boxplots of main results over 10 random runs. Each box summarizes the distribution across runs for three methods (ModelGPT, swab, ours).

NDCG@k. Define relevance $\text{rel}_\tau(m) \triangleq \text{rank}_\downarrow(r_\tau^*(m))$. Ordering \mathcal{I}_τ^k by $\hat{r}_\tau(m)$ as $(m_{(1)}, \dots, m_{(n)})$,

$$\text{NDCG}@k(\tau) \triangleq \frac{\sum_{i=1}^n \frac{2^{\text{rel}_\tau(m_{(i)})} - 1}{\log_2(i+1)}}{\text{IDCG}@k(\tau)}, \quad (55)$$

where $n = |\mathcal{I}_\tau^k|$ and IDCG@k(τ) is the ideal DCG@k.

$\tau@k$.

$$\tau@k(\tau) \triangleq \frac{C - D}{\binom{n}{2}}, \quad (56)$$

where C and D count concordant and discordant pairs between predicted and ground-truth ranks on \mathcal{I}_τ^5 .

Sum. $\text{Score}(\tau) \triangleq \text{NDCG}@5(\tau) + \tau@5(\tau)$.

F.3. Ground-Truth Rankings and Conductance Examples

To characterize how model performance changes with the evaluation data, we summarize the ground-truth ranking of all models on each dataset. Fig. 7 shows that the induced model order is not universal. We further visualize layer conductance patterns aggregated over all datasets for two representative models (Fig. 6), including coca-ViT-L-14 (laion2b_s13b_b90k) and xlm-roberta-base-ViT-B-32 (laion5b_s13b_b90k).

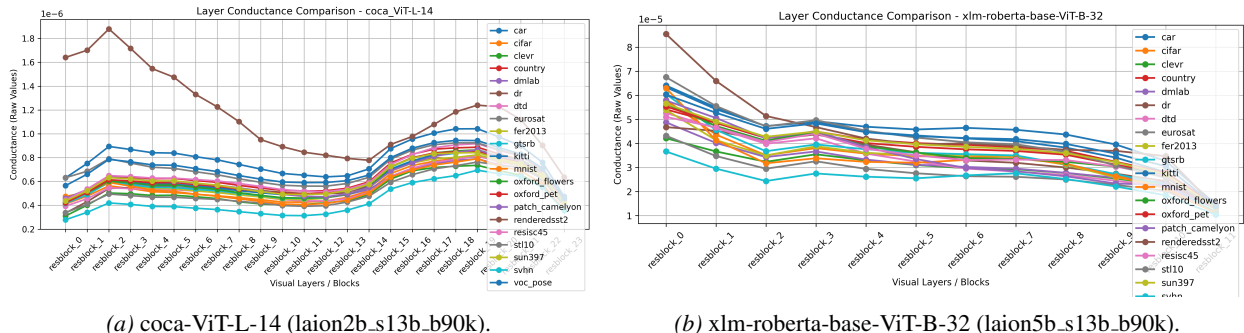


Figure 6. Layer conductance patterns aggregated over all datasets for two representative models.

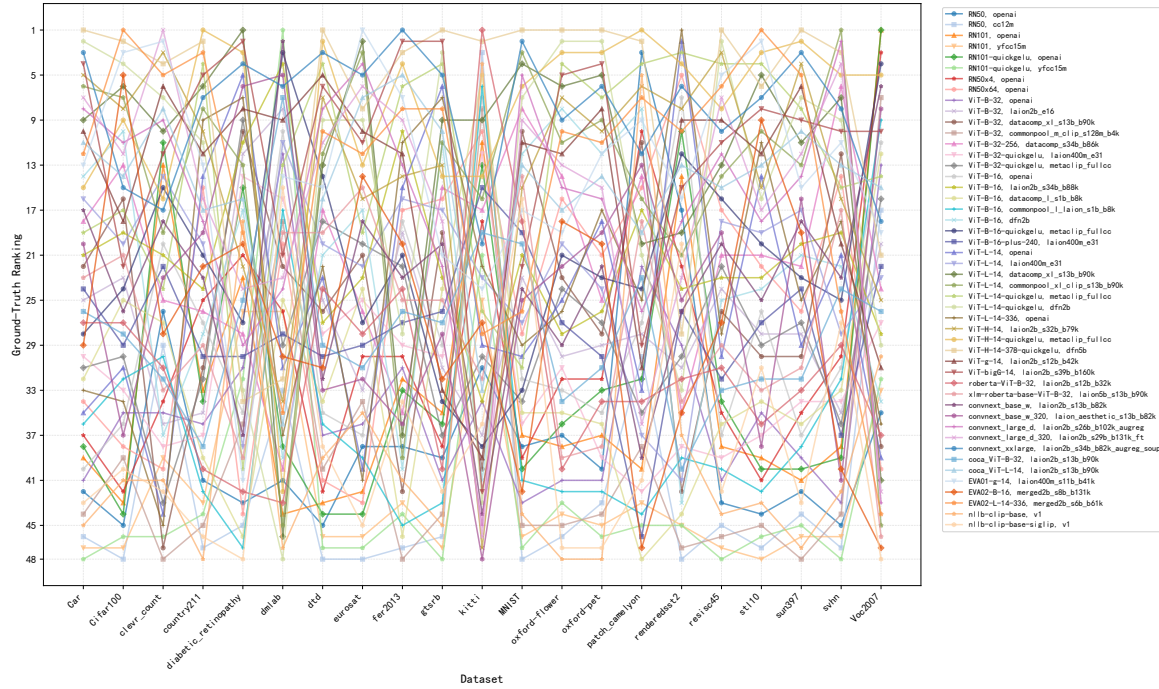


Figure 7. Ground-truth model ranking across all datasets. As can be seen, the ranking order varies across datasets.